Marek Jaszczur
Karolina Papis
Michał Książek
Grzegorz Czerwiński
Gabriel Wojtas
Wojciech Koncewicz
Sylwia Nabożna
Marcin Wójcik

INVESTIGATION OF AERODYNAMIC PARAMETERS OF SOLAR PLANE AIRFOIL USING CFD MODELING

Abstract

The technology of solar-powered aerial vehicles requires enormous financial support and further development. For this purpose, the computational fluid dynamic can be used. In order to carry out necessary analyses and model development in this research, ANSYS Fluent software was used. Using the first version of the AGH Solar Plane model, preliminary analysis of lift, drag and tearing off the stream was performed. Four new geometries were prepared on which the flattening of upper surfaces for fixing solar panels was tested. The results were validated in the aerodynamic tunnel using particle image velocimetry method. Taking into account all analyses, a number of recommendations have been prepared that will be implemented to create an aircraft, which meets all target requirements.

1. Introduction

The world today faces many difficult challenges, including environmental pollution, climate change, and energy crises. Due to this fact, the use of renewable energy is more and more popular – not only in the energy sector, but also to provide a power source for the transport sector. Solar energy is regarded as one of the most promising sources of energy for applications in the aerospace industry [24]. In contrast to conventional gasoline fuel-based planes, solar-powered planes convert solar energy directly into electrical energy by means of solar photovoltaic (PV) cells. Any surplus energy that is generated by solar cells can be stored in batteries, which allows for also carrying out flights at night [15, 26]. The first solar-powered airplane was Sunrise I, which was built in 1974. This plane weighed about 12 kg, and it took a flight that lasted 12 minutes at an altitude of 100 meters [1]. The power for the electric motor was generated by a bank of four solar photovoltaic arrays that were affixed to the upper airfoil surface. The cells had an average efficiency of 14% [3]. In 1980, Paul MacCready developed the Gossamer Penguin – the first manned aircraft that was powered entirely by PV panels. In 1981, he built a subsequent model with 16,000 solar cells on its wings. The cells were able to produce 2,500 watts of electrical power; however, this plane did not have the capacity for energy storage [12]. The turning point was the construction of the Solar Impulse 1 aircraft, which engaged in a multi-stage flight across the USA in 2013 [17]. With a wingspan of 72.3 m, its successor (Solar Impulse 2) made a remarkable achievement, which was a flight around the world. It flew at an average speed of 45 km/h [6]. To maximize the aerodynamic performance and optimize the energy chain, 11,628 monocrystalline silicon cells (each 150-microns thick) were mounted on the plane. It was important to maintain their lightness, flexibility, and solar cell efficiency (which reached as much as 22 %). For energy storage, lithium polymer batteries were used (whose energy density reached 240 Wh/kg). These batteries weighed 400 kg in total, which meant that they accounted for about 25% of the total weight of the aircraft [19]. The technology for unmanned solar-powered aerial vehicles requires enormous financial support and further development. The exact analytical solution of differential, integral, or integral-differential equations is limited to problems with simple geometries; thus, an approximate numerical solution is sought for most of the cases. For this reason, computational fluid dynamics (CFD) can be used to test and optimize newly designed solar-powered aerial vehicles. This is the most powerful technique for obtaining a large amount of very useful data. However, the used numerical models must be validated with a theoretical prediction or experimental measurement if CFD is to be reliable. At the same time, all three designing tools (theory, numerical modeling, and measurement) can be integrated in order to solve complex fluid flow problems and perform any required analyses [4].

Over the past few decades, several numerical simulations of solar planes have been performed [5, 13, 14]. It has been found that, at low angles of attack of the airfoil, the numerical results of the aerodynamic characteristics are obtained with relatively good accuracy and are in agreement with the experimental data [14]. Moreover, detailed

studies have allowed for the design of internal and external designs that are based almost exclusively on composite materials, achieving both desirable structural integrity and optimal aerodynamics [13]. In a large number of research studies [5, 25], it has been shown that the ANSYS Fluent solver can be accurate in the calculation of the lift coefficient; however, it has a lower precision when it comes to evaluating the drag coefficient [25]. In another work [2], the authors showed that, for a solar plane model, the maximum value of aerodynamic efficiency could be achieved for an angle of attack that is equal to 4°. In [16], the researchers compared the aerodynamic characteristics (XFOIL) of an airfoil with characteristics obtained by means of CFD analysis ($k - \omega$ SST and Transition SST). It turned out that the $k - \omega$ SST model cannot accurately resolve the actual phenomena that occur under low Reynolds number conditions. It can be also deduced that essential elements such as the laminar boundary layer separation, transition, and reattachment are properly captured by the Transition SST model. A mathematical model for a solar-powered aircraft and it preliminary design are presented in [18]. CFD was used in order to compare different geometrical configurations: a conventional aircraft, biplane aircraft, flying wing, and twin-boom aircraft. In [10], the authors focused on the flow characteristic around the airfoil of an unmanned aerial vehicle cruising at Re = 500,000. The proposed model was tested in a water tunnel and validated. The impact of the airfoil thickness and the different locations of the maximum thickness on the aerodynamic parameters were investigated. The presented results clearly show that the flow phenomena at a low Reynolds number is significantly affected by the laminar separation bubble. The location of the maximum thickness ought to be closer to the trailing edge, and the airfoil thickness should be as minimized as possible. The described methodology can also be a good guideline for airfoil design at low speeds. A flight strategy optimization model for solar-powered aircraft and its different configurations were investigated in [21]. The analyzed model includes an aerodynamic numerical model, an energy storage model, and a 3D kinematic model. In order to find an optimal solution, the Gauss pseudo-spectral technique was implemented. The presented analysis shows that the proper changes of a plane's attitude as well as the plane's angle contribute to photovoltaic cells power increases.

2. Scientific objective

The studies that have been conducted so far do not describe the aerodynamic parameters of the partially flat wings on which solar cells can be installed, but the characteristics of smoothed airfoils are always specified. In this work, the results of a typical airfoil modification on the essential aerodynamic parameters will be investigated. The purpose of this modification is to increase the available space for flat PV cells. The size of each flattened surface is determined by the dimensions of the photovoltaic cells. Moreover, to achieve their higher efficiency and to reduce economic costs, it is reasonable to use flat cells instead of flexible (elastic) ones. On the other hand, the uneven shape of a wing is supposed to obtain extra lift to a drag coefficient ratio of C_L/C_D. It is essential to find the optimal solution that could provide as high

a level of electrical efficiency as possible and good aerodynamic performance at the same time. Furthermore, the construction of an aerial vehicle is an individual case; in order to obtain the most reliable results, special investigations should be carried out.

3. Description of problem

In this research work, an airfoil dedicated for AGH Solar Plane construction [15] is optimized in order to maximize its lift-to-drag ratio C_L/C_D. In a solar plane, only the limited area of the airfoil is able to provide the efficient aerodynamic performance of the aircraft. Also, the nacelle should have a shape that generates as low a drag force as possible. To optimize the airfoil and to carry out all of the the necessary analyses, the Fluent solver was used. As a first step of analysis, a model geometry and computational domain were created. The geometry of the airplane was created in external packages (CAD, SolidWorks) and imported into the ANSYS DesignModeler module in order to clean the geometry and create the body parts that are required by the fluid flow solver. In most engineering problems, it is not possible to precisely reconstruct all of the details of the real geometry; hence, it is important to simplify the analyzed geometry but still keep all of the important details for the fluid phenomena. All of the details that are small and unimportant from a fluid-analysis point of view may cause significant difficulties during mesh generation. So, if their presence does not significantly affect the fluid flow, they should be avoided and removed. DesignModeler also allows for reducing the complexity of a model by generating symmetrical geometries (like a plane) "in half", which significantly reduces the calculation time. The three-dimensional (3D) model created in SolidWorks software is the simplified construction of a developed airplane with a wingspan that is equal to 3.0 m – this can be seen in Figure 1.
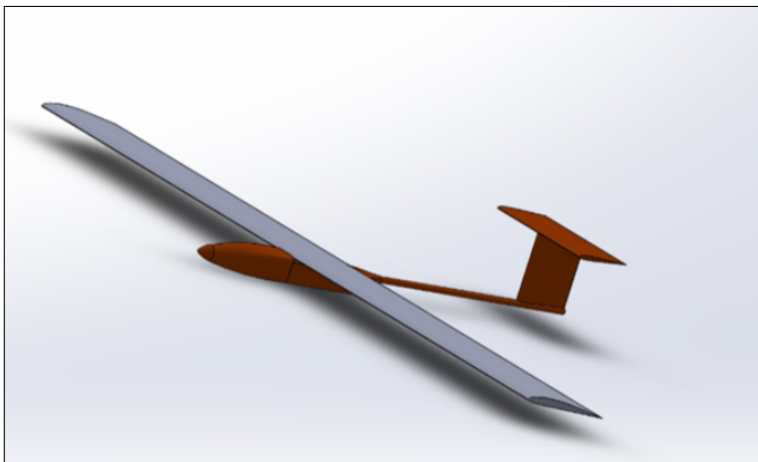

Figure 1. First analyzed model of airplane

For better control of the mesh-generation process, the model geometry was divided into several smaller bodies and multi-parts. The geometrical coordinates that describe the curve that creates the airfoil were imported in the details. In the DesignModeler module, a model parametrization was conducted in order to perform the optimization and run the calculations for various initial inputs. The second model of a nacelle (which can be seen in the Figure 2) was designed to minimize the drag force.
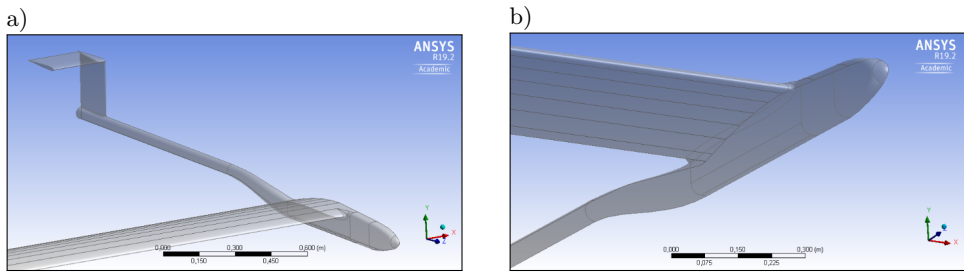
a)

b)

Figure 2. Second geometry of nacelle with wing and fins: half-body views from a) top and b) bottom

The main goal of this process was to reduce interference drag. The fuselage was curved down behind the wings to lower the drag that was created there. It also helped to obtain a greater lift force, as the airfoil was preserved throughout the whole length of the wing.Due to the airplane's geometrical and boundary-condition symmetry, only half of the model was ultimately analyzed in DesignModeler. In order to analyze the airplane, a domain that represents the surrounding fluid area is required. For this reason, an enclosure was added – it had a half-cylindrical shape with a rounded front and end. The radius of the computational domain was 10 meters, and the length was equal to 25 meters. The inlet air velocity vector was aligned with the connector of the fuselage and fins. In the next step, a numerical mesh was created. The mesh quality and its proper implementation has a crucial impact on the quality of the numerical results. An inadequate grid often makes calculations impossible to converge and generates results with very high numerical errors or physically incorrect values. This numerical grid-generation step takes much more time than the solver. A detailed investigation and verification of the grid-generation method (Tetrahedral Mesh, Sweep, Automatic, Multizone Meshing, and CutCell Meshing), the application of global mesh settings (e.g., selecting the maximum element size, mesh quality, and type of modeled phenomenon), and the local grid settings (the number of elements on a given edge as well as bias and inflation) were completed. In this work, all of the methods presented above were tested and verified, and the mesh quality was analyzed.The inflation setting was found to be essential for a current analysis, as it needs to resolve the boundary layer and keep a minimum orthogonal quality of at least 0.1 as well as a maximum skewness of no greater than 0.95. In this work, various settings were used for inflation to generate meshes with different heights of the first element on the airfoil, fins, and

nacelle that created a suitable y^+ parameter for all of the analyzed surfaces. To obtain a good quality mesh on the plane surfaces, the mesh face method and local face sizing were implemented. In addition, the mesh was refined in the region near the plane body using a function body of influence that had a geometrical shape that was similar to the computational domain but was approximately two-to-three-times smaller. In the next step, the types of the boundary conditions were defined. As a preliminary analysis showed that it was necessary to increase the mesh quality in the areas of the high-velocity gradient (such as the boundary layer, but also behind the airfoil and nacelle) in order to obtain accurate numerical results. Generating a good quality mesh has been found to have a crucial impact on the proper solution numerical error and fluid flow phenomena. All of the essential steps performed in this study are shown in Figure 3.
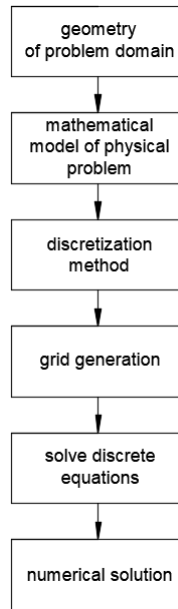

Figure 3. Sequence of steps for presented numerical simulation

Finally, the unstructured tetrahedral mesh method was used for the current model. The main reason for using this mesh method is the fact that the airplane has a complex geometry, and unstructured meshes are a good option. The mesh in the boundary layer was created using the inflation method. The number of layers in the boundary layer was set-up to 20, and the grow rate was equal to 1.2. The first layer height was set-up to $2.5 \cdot 10^{-3}$ m, giving an approximate average y^+ of between 30 and 50. In total, a mesh with approximately 1,900,000 nodes (middle mesh) was used in the main model calculations; however, two different grids were also tested: one with a two-times-higher number of points (fine grid), and one with a two-times-lower number of points (coarse

grid). The largest element size in the domain was equal to 0.4 m. The flow around the wing is important and will contain high pressure and velocity gradients, so this part was meshed with a local mesh size parameter that was equal to 0.002 m.

4. Mathematical model

To solve the fluid flow problem, governing equations are required. The Navier-Stokes equations for all three velocity components are fundamental equations for the fluid dynamics. Along with the continuity equation for unsteady phenomena in Cartesian coordinates x_i, these equations can be presented as follows [9]:

$$\frac{\partial \rho}{\partial t} + \frac{\partial \rho u_i}{\partial x_i} = 0 \tag{1}$$

$$\rho \frac{\partial u_i}{\partial t} + \rho u_k \frac{\partial u_i}{\partial x_k} = -\frac{\partial p}{\partial x_i} + \frac{\partial \tau_{ik}}{\partial x_k} \tag{2}$$

for $i = 1$, 2, and 3, where t is time, u is the fluid velocity component, p is the fluid pressure, and ρ is the fluid density. One of the most difficult issues in aerodynamics is the solution for fluid motions described by the Navier–Stokes equations. On the other hand, the industry requires a precise solution that would enable numerical testing of the product prior to experimental investigation. As direct solutions of Equations (1)–(2) are not possible to resolve turbulent flow for high Reynolds number flows, modeling must be introduced (as opposed to resolving the values directly). Therefore, the concept of Reynolds decomposition has been introduced, where the instantaneous variables in the Navier–Stokes equations are decomposed into mean and fluctuating parts [11]:

$$u = \overline{u} + u' \tag{3}$$

$$p = \overline{p} + p' \tag{4}$$

The relationships (Eqs. (3)–(4)) were implemented into the flow equations (Eqs. (1)–(2)); as a result, Reynolds averaged Navier–Stokes equations (RANS) were obtained as follows [23]:

$$\overline{u_j} \frac{\partial \overline{(u_i)}}{\partial x_j} = -\frac{1}{\rho} \frac{\partial \overline{p}}{\partial x_i} + \nu \frac{\partial \overline{u_i}}{\partial x_i x_j} - \frac{\partial \tau_{ij}}{\partial x_j} \tag{5}$$

$$\frac{\partial \overline{u_i}}{\partial x_i} = 0, \tag{6}$$

where ν is the fluid kinematic viscosity, and

$$\tau_{ij} = -\rho \overline{u_i' u_j'} \tag{7}$$

is the Reynolds stress term that incorporates the effects of turbulent motions on the mean stresses. The fluctuating components in Equation 7 are unknown. For this

reason, the system of the equation is not closed; therefore, additional properly selected model equations are required to solve the new unknown terms. Most of the turbulence models [8, 20, 22] are based on the Boussinesq hypothesis, which relates the Reynolds stress with the mean strain-rate tensor by the dynamic eddy-viscosity [7]. In this analysis, this hypothesis has also been implemented as follows:

$$\tau_{ij} = 2\mu_t S_{ij} - \frac{2}{3}\rho k \delta_{ij}, \tag{8}$$

and the mean strain rate tensor is as follows:

$$S_{ij} = \frac{1}{2}\left[\frac{\partial u_i}{\partial x_j} + \frac{\partial u_j}{\partial x_i}\right], \tag{9}$$

where k is the turbulent kinetic energy, u is the fluid velocity, μ_t denotes the dynamic eddy-viscosity, ρ is the fluid density, τ accounts for the shear stress, and σ_{ij} is the Kronecker delta. Simulations of the AGH Solar Plane were carried out using the Spalart–Allmaras turbulence model [9]; however, other turbulence models were also verified.

A high-quality mesh is essential for any accurate numerical calculation; however, numerical methods and implemented schemes also play important roles in ensuring low discretization error, stability, a fast solution, and convergence. Governing equations that are based on physics laws of conservation in the form of partial differential equations are integrated and solved for each element of the mesh based on the finite volume method. To obtain a solution, it was necessary to make some phenomena simplifications (geometrical) and constant properties (molecular viscosity). The validation of the numerical results was conducted by comparing the results that were obtained from the numerical simulations and results that were obtained in the wind tunnel by using enhanced particle image velocimetry (PIV) methods.

The SIMPLEC method was used to solve the analyzed problem. For the convective terms for spatial discretization, a second-order upwind scheme was used. The fluid (air) was modeled as an ideal gas.

5. Results

5.1. Model validation

In Figure 4, the three different meshes (coarse, medium, and fine) used in the validation process are shown. The numerical results for only the airfoil part are compared with the data that was obtained from the experimental PIV measurement for a few angles of attack. A comparison demonstrates the superior capabilities of the selected grid resolution. Both of the turbulence models considered in this work (Spalart-Allmaras and SST k-ω) predicted lift coefficient C_L with a relative error that was lower than 3% for a wide range of angles of attack (see Figure 5 for reference).
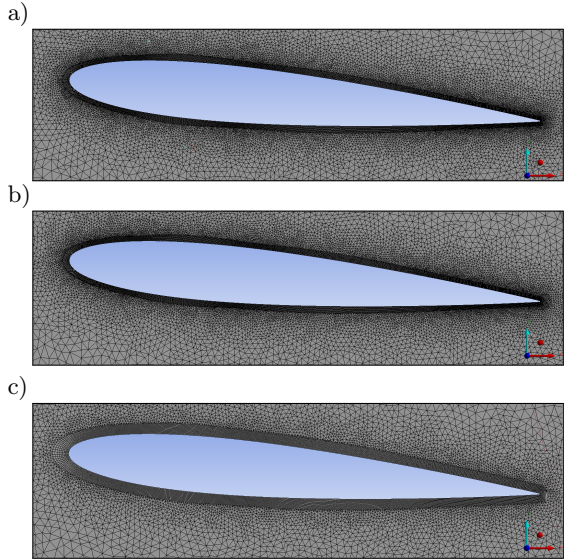
Figure 4. Different analyzed meshes for airfoil: a) fine; b) medium; c) coarse

It is clear from Figure 5 that the much simpler and faster Spalart-Allmaras turbulence model predicted lift coefficient C_L with the same accuracy (or even better) than with SST k-ω. For this reason, the solar plane analysis was performed using the Spalart-Allmaras turbulent model and a medium-sized resolution mesh.
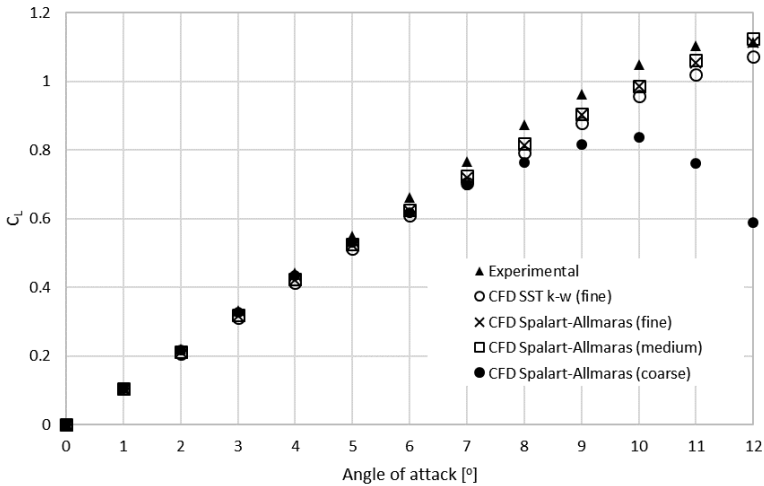

Figure 5. Airfoil lift coefficient C_L from experimental measurement and CFD analysis

5.2. First model

Using the "first version" model of the aircraft, a preliminary analysis of lift coefficient C_L and drag coefficient C_D was performed. During this analysis, aerodynamic parameters C_L and C_D were compared to the classic AG35 airfoil (shown in Figure 6) with a chord length that was equal to 0.32 m and calculated for various angles of attack.
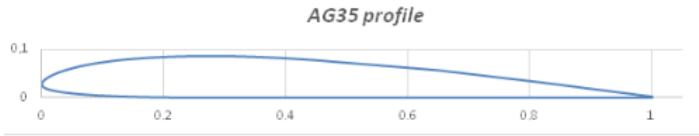

Figure 6. Airfoil model AG35

At the same time, the pressure and velocity distribution contours were investigated. In order to close the airfoil, the C-type domain was used with a circle (3.2-m radius) and rectangle (6.4-m length). In the ANSYS Meshing software, a hybrid mesh was created with local settings such as face meshing, bias, and edge sizing with a number of division that was equal to 100. The value of the y^+ parameter was about 30. In the ANSYS Fluent solver, the Spalart-Allmaras model of turbulence was used. Figure 7 shows the mesh that was generated to analyze the AG35-type-based airfoil and the airplane.
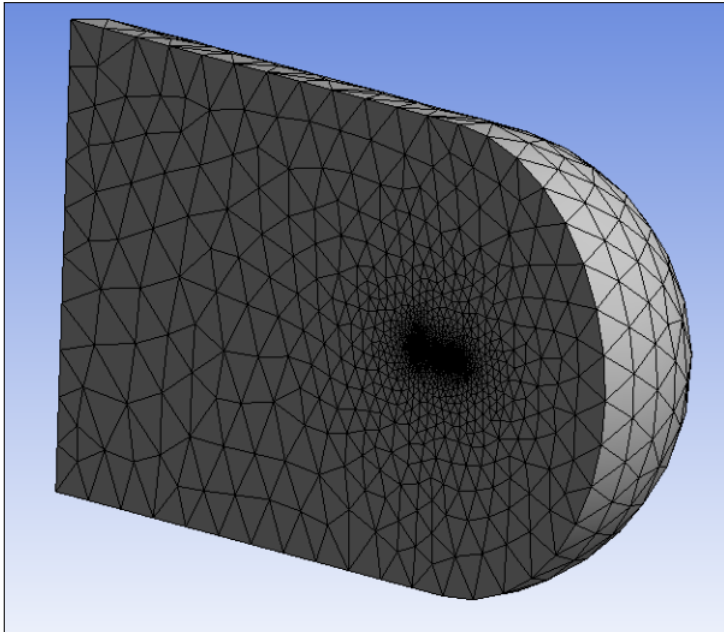

Figure 7. Mesh used for AG35 airfoil and first model of plane analysis

The results for lift coefficient C_L and drag coefficient C_D are presented in Figure 8, along with the reference values (scaled from a 1.0- to 0.32-meter-long chord).
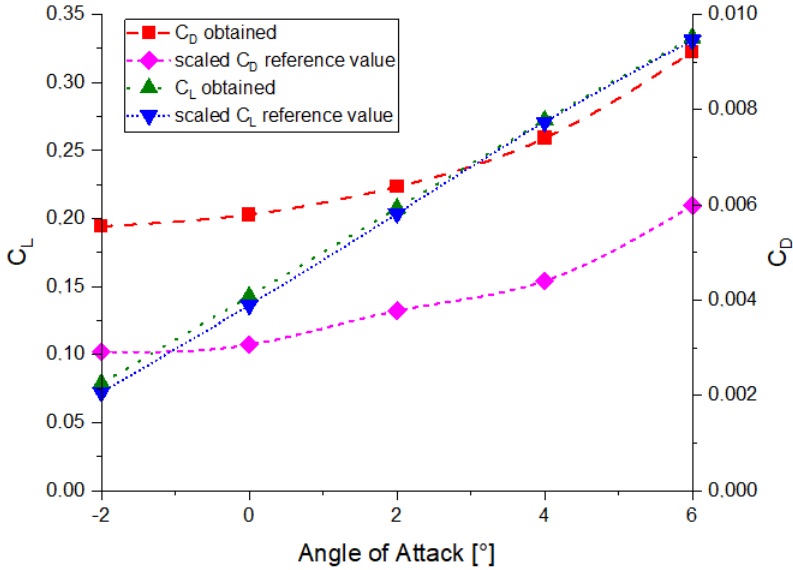

Figure 8. Calculated lift C_L and drag coefficient C_D for AG35 airplane wings

As can be seen from Figure 8, the trends are preserved with good accuracy, and the results of the simulation show the correct behavior. The pressure contour for an angle of attack that was equal to 0° is shown in Figure 9. The reference pressure is equal to the pressure calculated for 1 km above sea level, which was the target cruising altitude.
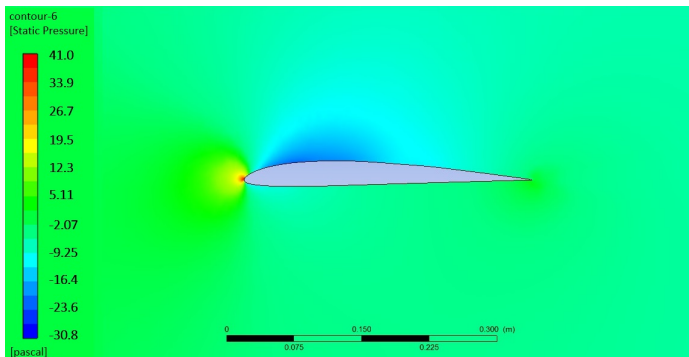

Figure 9. Distribution of pressure around airfoil for angle of attack equal to 0°

A region of low pressure is clearly visible above the upper surface of the airfoil (spreading from the front). At the tip of the airfoil, the point with the highest pressure is located.

Due to its symmetry, the geometry of the solar plane was limited to half for further use. In addition, the airplane's half-geometrical model was divided into four parts (fin, tail, wing, and dashboard); on each of these, various selected parameters for the mesh settings were investigated. Similar to the airfoil simulations, the geometry was placed inside a 3D C-shaped domain with a neutral position, giving a 0 angle between the inlet velocity vectors and the airfoil's edge of attack. In total, six simulations were carried out for different meshes and turbulence models. All of the results of the simulations generated similar results.
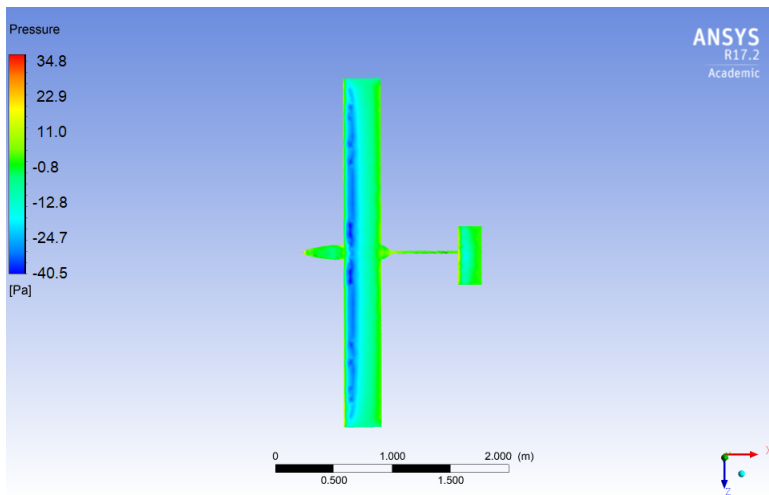

Figure 10. Distribution of pressure around plane for 0 ^{o} angle of attack

The maximum value of the lift force was from a calculation that was equal to 9.1715 N, which means that the total lift for the whole geometry was 18.3430 N. This is insufficient, as the anticipated value was 30 N.

Near the ends of the wings (where winglets are usually mounted), an area with higher pressure is located (see Figure 10). This leads to a reduction of lift force, so the geometry of the airfoil should be optimized in order to reduce the induced drag.

5.3. Second model

During the second stage of the study, airfoils with partially flattened surfaces were examined. The aim of these modifications was to create additional space for solar photovoltaic cells (which work at their highest efficiency when not twisted). As a reference airfoil, a Wortmann FX-60-100 was selected; it was then modified with

three, five, or six flat surfaces in order to represent PV cells. The airfoil profile and its modifications can be seen in Figure 11.
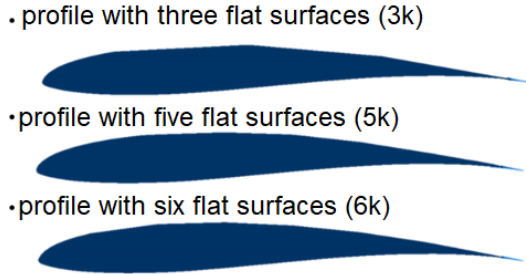

Figure 11. Modifications of classic airfoil profile

The analyzed airfoils have tails of 0.47 m in length. XFOIL software was used to examine the aerodynamic parameters of the airfoils. Analyses were carried out for velocities that were equal to 30 km/h, 40 km/h, and 50 km/h (which represented Reynolds numbers Re = 268,040, 357,386, and 446,733, respectively).

Figure 12 shows the lift-to-drag ratio depending on the angle of attack for a specified velocity of flight. On each chart, four airfoils are compared.

For each analyzed velocity of flight, the airfoil with three and five flat surfaces significantly varied from the reference ones. The lower values of the lift-to-drag ratio were obtained for angles of attack from 0 to 10. The most promising results were observed with the airfoil with six flat surfaces, as the maximum values were in good agreement with the reference ones. Table 1 presents the optimal angles of attack for each airfoil.

Table 1

Optimal angles of attack for various values of velocity and modifications of airfoils

Airfoil	$V = 30$ km/h	$V = 40$ km/h	$V = 50$ km/h
reference	5.0	4.7	4.4
three flat plains	3.6	4.1	7.4
five flat plains	4.7	4.3	3.9
six flat plains	3.8	2.6	4.8

The distribution of the pressure coefficients along the edges of the airfoil for the highest velocity are presented in Figure 13.
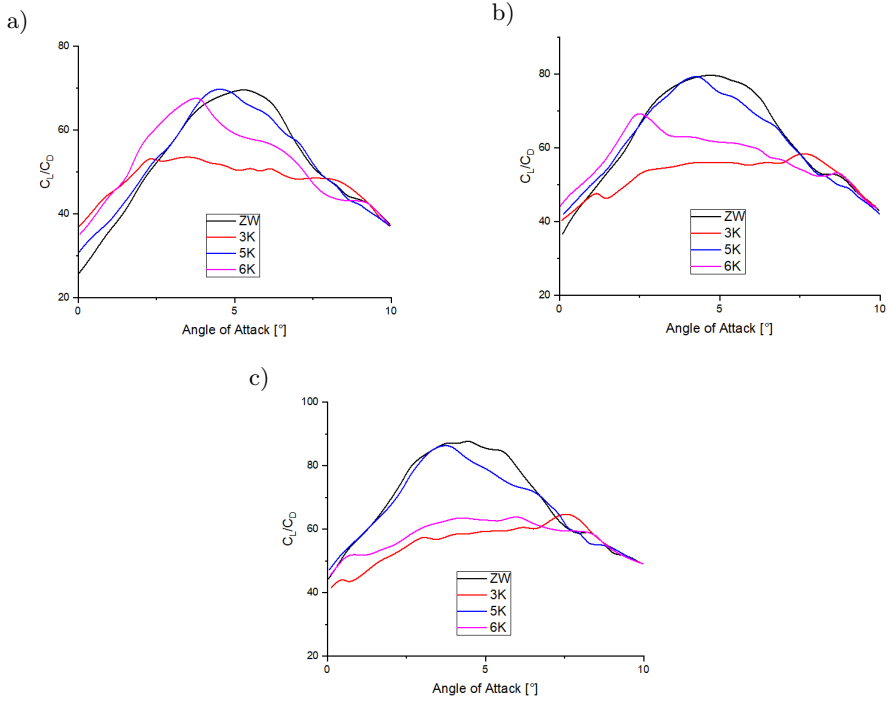
a)

b)

c)

Figure 12. Lift-to-drag ratios for various angles of attack and for different velocities of vehicle:
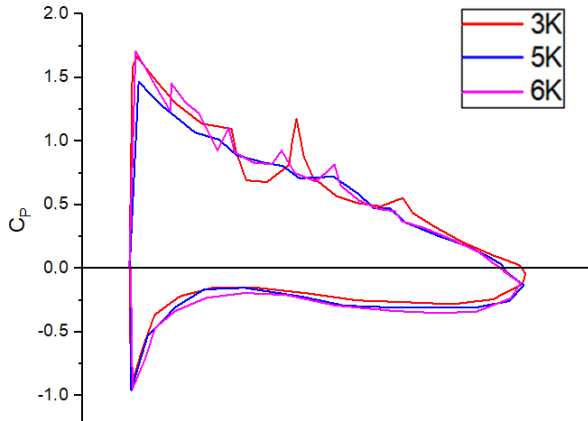a) 30 km/h; b) 40 km/h; c) 50 km/h

Figure 13. Pressure coefficient around airfoils with three, five, and six flat surfaces

In terms of their aerodynamic characteristics, the best characteristics were delivered by the airfoil with six flat surfaces, as the maximum lift-to-drag ratio for the

optimal angle is still comparable to the reference airfoil. For this airfoil, on the connections between the flat surfaces, peaks of under pressure are observed. If the number of panels (flat surfaces) is small (three surfaces in the analyzed case), then relatively large breakdown appears in the profile, causing local fluid flow instability; this is manifested by a step-change in the value of the C_p coefficient. This phenomenon occurs despite the very careful mapping of the profile geometry. These were significantly larger as compared to the other airfoil profiles. This can create dangerous forces that could detach any solar panels from a wing. The next step was to process the meshing of this domain. Structural and unstructural meshes were both generated with inflation layers around the body. Then, the boundary conditions were set as indicated in Table 2.

Table 2
Selected boundary conditions and their values

Boundary condition	Value	Unit
Velocity inlet	30	km/h
Turbulent viscosity ratio	10	–
Turbulent intensity	5	%
Pressure outlet	0	Pa
Wall plane surfaces	No slip, stationary	–
Symmetry	ZY Plane	–

Figure 14 shows velocity contours around the geometry at the symmetry plane. It is clearly visible that the area with the highest values is placed above the wing. Around the whole geometry, it can be seen that the velocity is zero; this is caused by the wall layer. Behind the tail of the plane, a region of the aerodynamic trace is located.
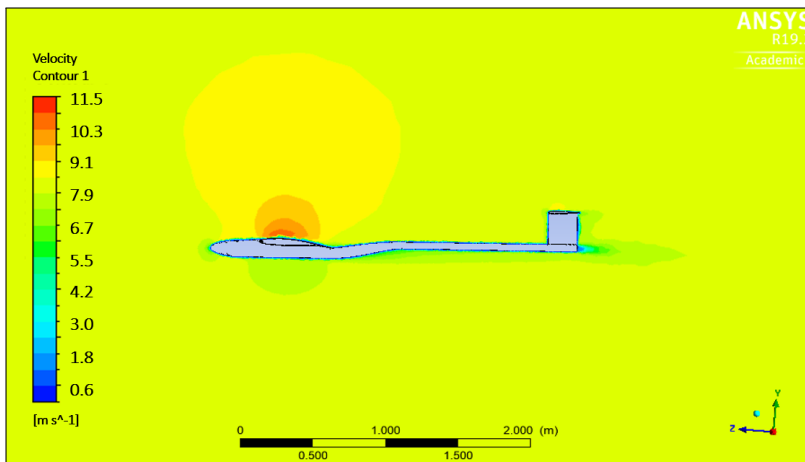

Figure 14. Contours of velocity around plane geometry

In Figure 15, the pressure gradient is shown. The consideration is the stagnation point in front of the nacelle, which was caused by the reduction of the local velocity of fluid when it came into contact with a locally perpendicular small part of the surface.
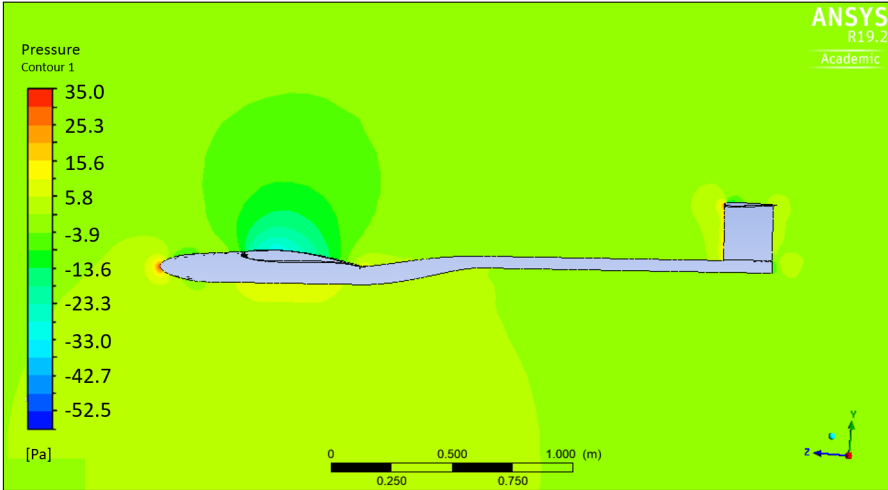

Figure 15. Contours of pressure around plane geometry

Figure 16 shows the contours of the pressure on the surface of the plane. In the area where there is a connection between the wings and the fuselage, there is a small area of raised pressure that was caused by the fillets; however, the design of the geometry ensures that the pressure gradient is as low as possible.
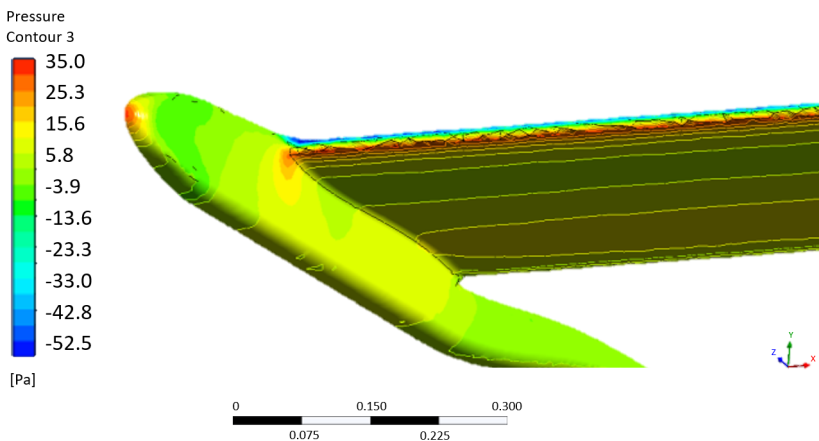

Figure 16. Contours of pressure on surface of plane geometry

It can be seen in Figure 17 that the kinetic energy of turbulence is reduced at the surface of the nacelle behind the wing, as the trailing edge ends at the top of the fuselage. This provides a minimization of the interference drag.
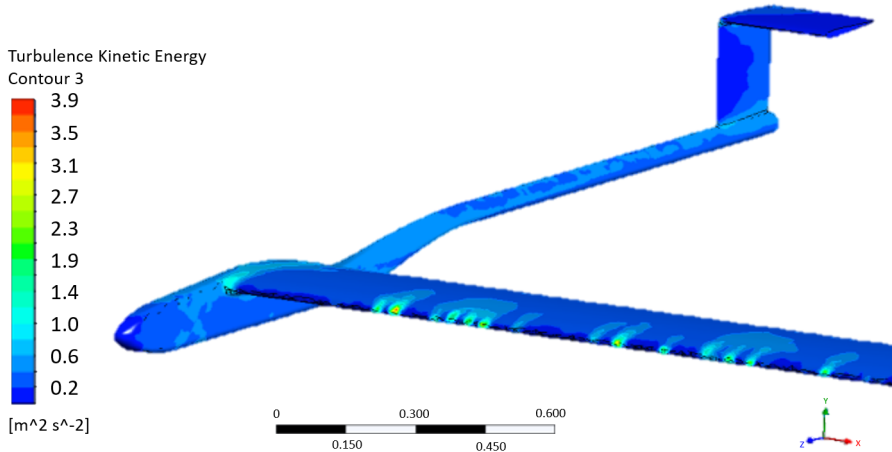

Figure 17. Contours of kinetic energy of turbulence on surface of plane geometry

6. Conclusions and future work

The studies presented here were carried out in order to analyze the aerodynamic parameters of the AGH Solar Plane at different speeds and angles of attack. The performed analysis provided an insight into important aspects of aerodynamic design, which should be taken into account when designing a solar plane. Taking all of the analyses into account, a number of recommendations have been prepared that will enable an aircraft to be created that meets all target requirements. It has been found that the proposed design for connecting the wing to the nacelle reduces the interference drag.This is due to the smoother connection between the wings and the nacelle in the second model of the airplane as compared to the first model. The airfoil flatness caused by the PV flat cells decreased the C_L to C_D ratio. However, a significant drop could be observed for mainly the wings with three and five flat plains. The results for six flat plains were very similar to the non-flat plain result; only small differences were observed for angles of attack that were greater than 5°. The steepest decrease could be seen for the optimal angle of attack; in some cases for the wing with three flat plains, the C_L/C_D was approximately 40% in reference to the non-flat plain. In a further analysis of the complete AGH Solar Plane, a geometry with more details and an engine will be investigated. Winglets will also be considered as elements that can generate more-homogeneous pressure at the airfoil's upper surface. This will require a much finer grid to resolve all of the geometrical details.

Acknowledgements

References

[1] Abbe G., Smith H.: Technological development trends in Solar-powered Aircraft Systems, *Renewable and Sustainable Energy Reviews*, vol. 60, pp. 770–783, 2016.

[2] Betancourth N.J.P., Villamarin J.E.P., Rios J.J.: Design and Manufacture of a Solar-Powered Unmanned Aerial Vehicle for Civilian Surveillance Missions, *Journal of Aerospace Technology and Management*, vol. 8, pp. 385–439, 2016.

[3] Boucher R.: Project Sunrise, *Astro Flight Inc*, 1975.

[4] Cebeci T., Shao J.P., Kafyeke F., Laurendeau E.: *Computational Fluid Dynamics for Engineers*, Springer-Verlag, Berlin–Heidelberg, 2005.

[5] Chen J., Wang Z., Zhang J., Zhang L., Wu G.: Numerical Simulation for Changes in Aerodynamic Characteristics Along the Spanwise of "Diamond Back" Wing, *Procedia Engineering*, vol. 99, pp. 566–574, 2015.

[6] Dawson D.: Solar Impulse 2: Pulse on the future, *Composites World*, vol. 71, pp. 36–53, 2016.

[7] Gatski T.B., Speziale C.G.: On explicit algebraic stress models for complex turbulent flows, *Journal of Fluid Mechanics*, vol. 254, pp. 59–78, 1993. doi:10.1017/S0022112093002034.

[8] Jones W.P., Launder B.E.: The prediction of laminarization with a two-equation model of turbulence, *International Journal of Heat and Mass Transfer*, vol. 15(2), pp. 301–314, 1972. doi:10.1016/0017-9310(72)90076-2.

[9] Li Q., Ma Q.W., Yan S.: Investigations on the future of turbulent viscosity associated with vortex shedding, *Procedia Engineering*, vol. 126, pp. 73–77, 2015.

[10] Ma D., Zhao Y., Qiao Y., Li G.: Effects of relative thickness on aerodynamic characteristics of airfoil at a low Reynolds number, *Chinese Journal of Aeronautics*, vol. 28, pp. 1003–1015, 2015.

[11] Nguyen C.: Turbulence Modeling, 2005. http://web.mit.edu/~cuongng/www/Site/Publication˙files/TurbulenceModeling˙04NOV05.pdf.

[12] Noth A., Siegwart R., Engel W.: Design of Solar Powered Airplanes for Continuous Flight, *Environmental Research*, vol. 18, 2007.

[13] Panagiotou P., Giannakis E., Savaidis G., Yakinthos K.: Aerodynamic and structural design for the development of a MALE UAV, *Aircraft Engineering and Aerospace Technology*, vol. 90, pp. 1077–1087, 2018.

[14] Panagiotou P., Tsavlidis I., Yakinthos K.: Conceptual design of a hybrid solar MALE UAV, *Aerospace Science and Technology*, vol. 53, pp. 207–219, 2016.

[15] Papis K., Figaj R., Kuś J., Żołądek M., Zając M.: Application of photovoltaic cells as a source of energy in unmanned aerial vehicle (UAV) – case study, *E3S Web of Conferences*, vol. 173, 2020.

[16] Park D., Lee Y., Cho T., Kim C.: Design and Performance Evaluation of Propeller for Solar-Powered High-Atitude Long-Endurance Unmanned Aerial Vehicle, *International Journal of Aerospace Engineering*, pp. 1–23, 2018.

[17] Rajendran P., Smith H.: Development of Design Methodology for a Small Solar-Powered Unmanned Aerial Vehicle, *International Journal of Aerospace Engineering*, p. 10, 2018.

[18] Rizzo E., Frediani A.: A model for solar powered aircraft preliminary design, *The Aeronautical Journal*, vol. 112, pp. 57–78, 2008.

[19] Solar Impulse: Around the World in a Solar Airplane, 2016.

[20] Spalart P.R., Allmaras S.R.: A one-equation turbulence model for aerodynamic flows, *AIAA*, pp. 1–22, 1992.

[21] Wang S., Ma D., Yang M., Zhang L., Li G.: Flight strategy optimisation for high--altitude long-endurance solar-powered aircraft based on Gauss pseudo-spectral method, *Chinese Journal of Aeronautics*, vol. 32, pp. 2286–2298, 2019.

[22] Wilcox D.C.: Reassessment of the scale-determining equation for advanced turbulence models, *AIAA Journal*, vol. 26(11), pp. 1299–1310, 1988. doi:10.2514/3.10041.

[23] Woelke M.: Eddy Viscosity Turbulence Models emploed by Computational Fluid Dynamic, *Prace Instytutu Lotnictwa*, vol. 4, pp. 92–113, 2007.

[24] Xian-Zhong G., Zhong-Xi H., Zheng G., Xiao-Qian C.: Reviews of methods to extract and store energy for solar-powered aircraft, *Renewable and Sustainable Energy Reviews*, vol. 44, pp. 96–108, 2015.

[25] Xian-Zhong G., Zhong-Xi H., Zheng G., Xiong F., Jian-Xia L., Xiao-Qian C.: Parameters determination for concept design of solar-powered, high-altitude long-endurance UAV, *Aircraft Engineering and Aerospace Technology*, vol. 85, pp. 293–303, 2013.

[26] Xiongfeng Z., Zheng G., Zhongxi H.: Solar-powered airplanes: A historical perspective and future challenges, *Progress in Aerospace Sciences*, vol. 71, pp. 36–53, 2014.

Affiliations

Marek Jaszczur
   AGH University of Science and Technology, Krakow, jaszczur@agh.edu.pl

Karolina Papis
   AGH University of Science and Technology, Krakow, papis@agh.edu.pl

Michał Książek
   AGH University of Science and Technology, Krakow, miksiaze@student.agh.edu.pl

Grzegorz Czerwiński
    AGH University of Science and Technology, Krakow, czerwyrz@student.agh.edu.pl

Gabriel Wojtas
    AGH University of Science and Technology, Krakow, gabriel@student.agh.edu.pl

Wojciech Koncewicz
    AGH University of Science and Technology, Krakow, wkon@student.agh.edu.pl

Sylwia Nabożna
    AGH University of Science and Technology, Krakow, snabozna@student.agh.edu.pl

Marcin Wójcik
    AGH University of Science and Technology, Krakow, wojcikm@student.agh.edu.pl